Monitoring the morphological changes of Si-based electrodes by X-ray computed tomography: A 4D-multiscale approach

Victor Vanpeene, Julie Villanova, Jussi-Petteri Suuronen, Andrew King, Anne Bonnin, Julien Adrien, Éric Maire, Lionel Roue

Monitoring the morphological changes of Si-based electrodes by X-ray computed tomography: A 4D-multiscale approach

V. Vanpeene[a,b], J. Villanova[c], J.P. Suuronen[c], A. King[d], A. Bonnin[e], J. Adrien[b], E. Maire[b], L. Roué[a,*]

[a] *Institut National de la Recherche Scientifique (INRS) - Centre Énergie, Matériaux, Télécommunications (EMT), J3X 1S2 Varennes (QC) Canada.*

[b] *MATEIS - CNRS UMR 5510 INSA Lyon, F-69621 Villeurbanne, France.*

[c] *ESRF-The European Synchrotron, ID16B, F-38000 Grenoble, France.*

[d] *Synchrotron Soleil, Psiché beamline, F-91190 Gif-sur-Yvette, France.*

[e] *SLS facility, Tomcat beamline, Paul Scherrer Institut, S-5232 Villigen, Switzerland.*

* Corresponding author:

E–mail: roue@emt.inrs.ca (L. Roué)

Abstract

Visualization and quantification of the morphological changes of Si-based electrodes occurring upon cycling are essential for better understanding their degradation mechanism and for optimizing their formulation. In this context, *in-situ* and *ex-situ* X-ray computed tomography (XRCT) analyses are here performed on Si-based electrodes for different cycling steps and at different scales (*i.e.* from the composite electrode level down to the Si particle one). Three different cell configurations and four different X-ray sources (one laboratory and three synchrotrons) have been used and their impact on the image resolution/quality and the segmentation of the different solid, electrolyte and gas phases of the composite electrodes is highlighted. From these complementary XRCT analyses with a voxel size ranging from 0.8 to 0.05 μm, key morphological features have been studied such as *(i)* the volume expansion/contraction of the electrode, *(ii)* the dynamics of the electrode macrocracking, *(iii)* the initial solid electrolyte interphase (SEI) layer growth and related formation of gas and consumption of electrolyte, which strongly depend on the presence of fluoroethylene carbonate in the electrolyte, *(iv)* the evolution of the electrode porosity and macrocrack volume fraction/connectivity/width after prolonged cycling.

Keywords: Li-ion batteries; silicon anode; morphological degradation; X-ray tomography;

1. Introduction

Li-ion battery electrodes have a complex porous 3D microstructure constituted of a network of active material particles and conductive additive connected together, and to the current collector, thanks to a binder. The porous network between the solid particles, allowing the electrolyte to access to the active material, also plays a key role in the electrode performance. Simulated analyses run in 3D and modelling have shown that the shape, the tortuosity, and the surface area of pores and active particles are all key parameters for the improvement of electrode performances **[1-6]**. Moreover, these complex 3D networks must be maintained upon cycling in order that all the active material particles remain electrochemically active and contribute to the electrode capacity. This is particularly challenging for high-capacity alloying anode materials such as silicon that undergoes a huge volume change upon its lithiation (up to ~280% **[7]** compared to only ~10% for a conventional graphite anode). This leads to the disintegration of the electrode architecture (cracking, collapse, and/or peeling-off), which results in a poor electrode cycle life **[7]**. Another key aspect affecting the cycle life of silicon based electrodes is the instability of the solid electrolyte interphase (SEI) **[8,9]**.

Hence, new challenges lay in the manner of measuring Li-ion electrode morphological changes occurring upon cycling, especially at a very small length scale and in 3D. Recently, different imaging techniques have been used to study various Si-based electrodes, like scanning transmission electron microscopy (STEM) **[10,11]**, focused ion beam/scanning electron microscopy (FIB/SEM) tomography **[12,13]**, and X-ray computed tomography (XRCT) **[14-24]**. The XRCT is the most versatile technique offering a large range of spatial resolution depending on the X-ray source and the setup used. Even if STEM provides a better resolution, XRCT allows the

observation of electrode material in a more representative way thanks to the 3D quantitative information extracted on larger field of view and with less sample preparation. Compared to FIB/SEM tomography, XRCT is a non-destructive characterization technique. Thus, *in-situ* acquisition can be performed with an appropriate electrochemical cell in order to assess the morphological evolution of the electrode upon cycling. The XRCT spatial resolution is determined by different parameters such as pixel size of the detector, but also, for a conical beam configuration, by the X-ray spot size, which depends on the X-ray source and the source-sample working distance. Micrometric spatial resolution is usually obtained with a conventional laboratory X-ray source whereas tens of nm resolution can be reached using a synchrotron X-ray source. Moreover, the highly coherent and bright synchrotron X-ray beams are of special interest to perform phase contrast imaging in order to distinguish materials of low and/or similar X-ray attenuation, which are very common in the Li-ion battery field (*e.g.* carbon, silicon and electrolyte have similar attenuation coefficients) **[25]**.

In the present study, the morphological changes induced by cycling of Si-based electrodes are studied by *in-situ* and *ex-situ post-mortem* XRCT analyses performed at different scales (from the composite electrode scale to the Si particle one) and with different voxel sizes (ranging from 0.8 µm to 50 nm). For that purpose, different X-ray sources and electrochemical cell configurations are used and their impact on the XRCT image resolution is highlighted. The main morphological features of the Si-based electrodes observable at different length-scales and varying with cycling are presented and discussed.

2. Experimental

2.1. Electrode composition and preparation

Five Si-based electrodes were characterized by XRCT as listed in **Table 1**. In all cases, the composite electrodes were constituted of 80%^{wt} of active material, 12%^{wt} of conductive additive and 8%^{wt} of binder. The active material was Si powder obtained by high-energy ball milling of commercial Si powder (99.999%, 20 mesh, Materion) for 20 h under argon atmosphere using a SPEX 8000 mixer with a ball-to-powder mass ratio of 5:1. The as-milled Si powder consists in micrometric agglomerates made of sub-micrometric particles more or less agglomerated together. More details on the characteristics of the as-milled Si powder are presented elsewhere **[26]**. There is a de-agglomeration of the as-milled Si powder during the slurry (ink) mixing and the size of the resulting Si powder in the electrode depends on the slurry mixing procedure (see below). The median diameter of the Si particles (D_v50) was 0.8 µm for electrodes #1, #3 and #5, and 2.4 µm for electrodes #2 and #4. Their respective particle size distribution (PSD) curves are shown in supplementary **Fig. S1**. The use of larger Si particles makes easier their identification (segmentation) by XRCT. For all electrodes, the binder was the carboxymethyl cellulose (CMC) (DS = 0.7, Mw = 90 000 g mol^{-1}, Sigma-Aldrich). For electrodes #3 and #4, the conductive additive was carbon black (CB) (Super P grade from Imerys Graphite & Carbon, particle size ~40 nm, S_{BET} = 62 m^2 g^{-1} according to the supplier's data). For electrodes #1, #2 and #5, the conductive additive was graphene nanoplatelets (GnP) (M grade from XGSciences, average diameter = 15 µm, average thickness = 6-8 nm, surface area = 120-150 m² g^{-1} according to the supplier's data). Our recent works have shown that GnP as conductive additive offers better cyclability for Si-based electrodes than usual CB **[24,27]**.

A slurry was prepared by mixing 200 mg of 80%^{wt} Si, 8%^{wt} CMC and 12%^{wt} GnP or CB added in 0.5 mL pH3 buffer solution. The use of a buffered pH3 solution instead of neutral water as slurry medium increases the efficiency of the CMC binder by promoting the formation of covalent bonds between -OH groups present on the Si particles and -COOH groups of CMC, which improves the mechanical strength and cycling performance of the electrode **[28,29]**. The slurry mixing was performed at 500 rpm for 1 h using a Fritsch Pulverisette 7 mixer with 3 silicon nitride balls (9.5 mm diameters) or by using a magnetic stirrer. With the former mixing procedure, the de-agglomeration of the as-milled Si powder is more efficient, resulting in a Si median size of 0.8 µm compared to 2.4 µm by magnetic stirring as previously indicated.

Except for electrodes #4, a 3D carbon paper (AvCarb EP40, Fuel Cell Store) was used as substrate. The first reason of the choice of a carbon paper as substrate is that it enables proper X-ray tomographic imaging of the electrode without creating metal artefacts due to the hardly attenuating behavior of the conventional copper foil current collector. Additionally, the flexibility and 3D geometry of the carbon paper helps to maintain the electrical connections during cycling **[22,24]**. The EP40 carbon paper consists in non-woven carbon fibers (~10 µm diam.) bound by a binder filled with micrometric carbon particles. According to its characterization by standard laboratory XRCT, its mean thickness is 144±15 µm and its mean porosity is ~82% with a median pore size of 36 µm (see ref. **[22]** for more details). The carbon paper (3 or 1 mm diam. disc depending on the electrochemical cell used, see below) was loaded with the Si-based slurry as described in ref. **[22]**. For electrodes #4, another approach was used for the electrode preparation, which is more suitable for local tomography at high resolution. In this case, the slurry was deposited on the tip (~100 µm diam.) of a conically machined copper wire. In all cases, the electrode was dried for 12 h at room

temperature and then at 100°C under vacuum for 2 h. The areal Si mass loading of the electrodes was between 1.4 and 4.5 mg_{Si} cm^{-2} (**Table 1**).

	Electrode composition (%wt)	Electrode loading (mg_{Si} cm^{-2})	Median Si particle size (µm)	Substrate	Electrode diameter (mm)	Cycling conditions	X-ray source	Imaged volume ($µm^3$)	Voxel size (µm)
#1	Si/GnP/CMC (80/12/8)	1.8	0.8	C paper	1	1 cycle at C/9 in LP30+FEC	Lab. source	1358 ×1358 × 200	0.80
#2	Si/GnP/CMC (80/12/8)	2.6	2.4	C paper	3	1 cycle at C/9 in LP30+FEC	Soleil Psiché	943 × 943 × 208	0.65
#3	Si/CB/CMC (80/12/8)	1.4	0.8	C paper	3	1.5 cycle at C/9 in LP30	SLS Tomcat	293 ×293 × 137	0.16
#4	Si/CB/CMC (80/12/8)	~4.5	2.4	Cu tip	0.2	~1.5 h of discharge at C/20 in LP30 and LP30+FEC	ESRF ID16B	128 ×128 × 108	0.05
#5	Si/GnP/CMC (80/12/8)	1.8	0.8	C paper	1	Ex-situ XRCT after 0, 30 and 50 cycles at C/9 in LP30+FEC	ESRF ID16B	128 ×128 × 108	0.05

Table 1. *Experimental details on the Si-based electrodes analysed by XRCT*

2.2. Electrochemical cells and cycling conditions

The three electrochemical cells used for the *in-situ* XRCT performed at different length scales are presented in **Fig. 1a-c**. These are all a cylindrical shape and in two-electrode configuration with Si-based electrode as working electrode and a Li foil as counter and reference electrode. The first cell with polytetrafluoroethylene (PTFE) cell housing was used for laboratory XRCT on electrode #1 (**Fig. 1a**), where the cell cylinder (1.2 mm outer diam. cell, 1 mm diam. electrode) needs to be as thin as possible in order to reach sufficient resolution by pushing the cell closer to the X-ray source. The second cell, with perfluoroalkoxy alkane (PFA) cell housing, is larger (8.2 mm outer diam. cell, 3 mm diam. electrode) (**Fig. 1c**). A slight compression was applied by a spring placed on the counter electrode side in order to keep better contact between the cell components. This compression leads to a gentle reduction of the C paper electrode thickness from ~140 µm before cell assembling down to ~100 µm after cell assembling. It was used with electrodes #2 and #3 on the synchrotron radiation beamlines as the

diameter of the cylinder is less critical for reaching high resolution. However, to reach a resolution as high as 0.05 µm, a smaller electrode cell (1.2 mm outer diam. cell) (**Fig. 1b**) was used for synchrotron XRCT on electrodes #4. Moreover, in this cell, the size of the electrode was reduced as low as possible by using a conically machined Cu wire as substrate (0.2 mm diam. electrode including the Si-based coating). The cells were assembled in an argon filled glove box. At the exception of the conical electrode cell, a borosilicate glass-fiber (Whatman GF/D) was used as a separator and was soaked with the electrolyte.

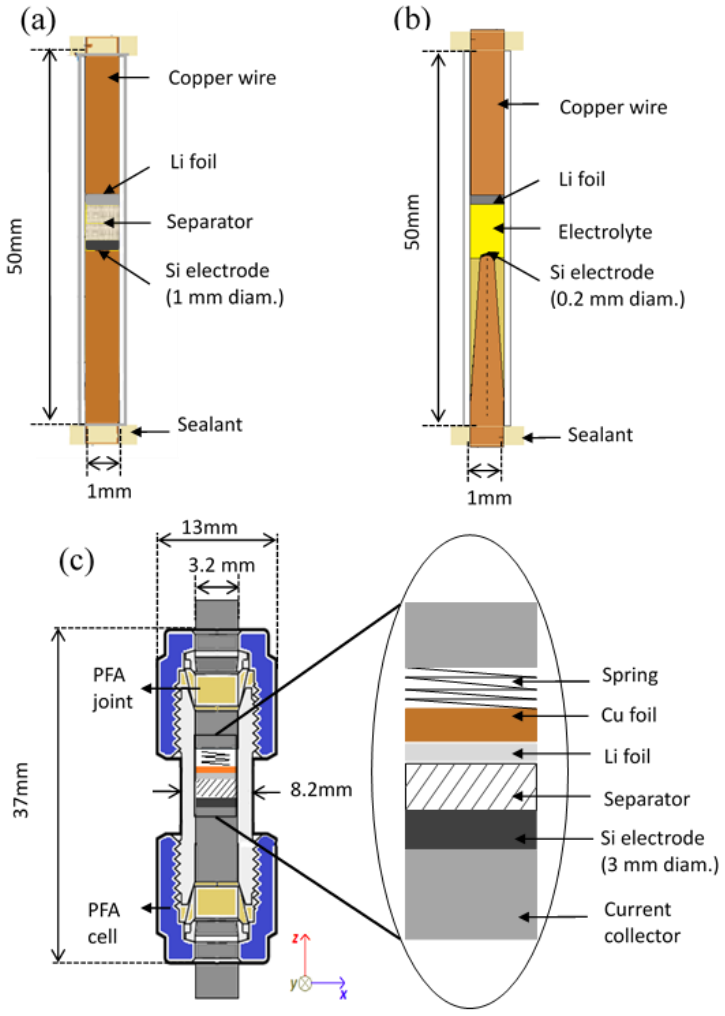

***Figure 1**. Schematic representation of the electrochemical cells used for in-situ laboratory (a) and synchrotron (b,c) XRCT.*

The electrochemical cells were fixed on a rotating stage with their axis aligned along the rotation axis of the tomograph and connected to a potentiostat/galvanostat (OrigaFlex OGF500). The electrodes were cycled at room temperature in 1 M $LiPF_6$ in ethylene carbonate (EC) and dimethyl carbonate (DMC) (1:1) (LP30) with 10%^{wt} fluoroethylene carbonate (FEC). The electrode #3 and one of the electrodes #4 were cycled in LP30 electrolyte without FEC in order to study the impact of the electrolyte additive on the SEI formation. Cycling was performed in galvanostatic mode at full capacity between 1 V and 5 mV *vs.* Li^+/Li at a constant current density of 400 mA g^{-1} of Si (C/9) for electrodes #1 to #3 and 180 mA g^{-1} of Si (C/20) for the two electrodes #4 in both discharge (lithiation) and charge (delithiation). The cell was imaged at regular time intervals during the first charge and discharge, except for electrodes #4 where XRCT acquisitions were restricted to the early stage of lithiation (~1.5 h) to emphasize the SEI formation. During the XRCT acquisition periods, the cell was let to the open circuit potential.

Additionally, *ex-situ* synchrotron XRCT (*i.e.* after cell disassembly) were performed on electrodes #5 after 30 and 50 cycles at a constant current of 400 mA g_{Si}^{-1} (C/9) in LP30 + 10%^{wt} FEC with a conventional two-electrode Swagelok-type cell (1 cm diam.) and compared to their pristine state. The cycled electrodes were rinsed for 10 minutes in a dimethylcarbonate (DMC) solution to eliminate the remaining trace of electrolyte and then cut in 1 mm diam. samples. The samples were not exposed to air until the XRCT scanning, where they stayed ~3.5 h exposed to the room atmosphere conditions.

2.3. X-ray sources and image acquisition procedure

Four different X-ray sources were used for the XRCT measurements: one lab source and three synchrotron sources, namely *(i)* the Psiché beamline of the SOLEIL facility in Gif-sur-Yvette (France), *(ii)* the Tomcat beamline of the Swiss Light Source (SLS) facility at the Paul Scherrer Institut (Villigen, Switzerland) and *(iii)* the ID16B beamline of the European Synchrotron Radiation Facility (ESRF) in Grenoble (France). The main specific features of each X-ray source are listed in **Table 2**.

X-ray source	E (keV)	ΔE/E	Flux Φ (ph s^{-1})	Brightness (ph s^{-1} mm^{-2} $mrad^{-2}$ 0.1%BW)
Lab. source	~10	~10^{-1}	~10^{8}	<10^{8}
Soleil Psiché	25	~10^{-2}	~10^{13}	~10^{19}
SLS Tomcat	20	~10^{-2}	~10^{14}	~10^{19}
ESRF ID16B	17.5	~10^{-2}	~10^{12}	~10^{21}

Table 2*. Specific features of the X-ray sources*

The laboratory XRCT experiments (performed on electrode #1) were achieved using an EasyTom (Rx Solutions) with a LaB_6 cathode (E = 76 kV, I = 96 µA, spot size down to 0.25 µm) and a CCD Hamamatsu 4000 × 2624 pixels detector available at the MATEIS laboratory at INSA-Lyon, France. In this set up of conical X-ray beam, the sample-source distance (and the sample-detector distance) determine the reachable voxel size and it cannot be smaller than the physical size of the source because of the so-called "geometrical blur". Therefore, it is of particular importance to design the smallest reasonably possible electrochemical cell to decrease the sample/source distance and hence the voxel size. With our 1.2 mm diameter electrochemical cell (**Fig. 1a**), a voxel size of 0.8 µm was reached for a reconstructed electrode volume of 1358 × 1358 × 200 $µm^3$. The images were taken continuously (on the fly) during the sample rotation without any averaging, thus the total acquisition time was reduced to 17 min

per scan compared to 55 min for a standard triggered scanning procedure (see **Fig. S2** and related comments in supplementary information for more details).

Higher resolution is mandatory for the observation of the phenomena occurring at a small length scale in the electrode and for the precise quantitative analysis of the electrode morphology. The image quality for reaching high resolution relies on the source brightness defined as:

$$B \propto \frac{\Phi}{\sigma_x.\sigma_y.\delta\theta_x.\delta\theta_y} \text{ (ph s}^{-1}\text{ mm}^{-2}\text{ mrad}^{-2}\text{ 0.1\%BW)} \quad (1)$$

where Φ is the photon flux, σ_x, σ_y, $\delta\theta_x$, $\delta\theta_y$ are the lateral source size and the angular spreads. BW is the bandwidth defined as the dispersion of the wavelength from the targeted value. A conventional X-ray source does actually not match the requirements for high brightness: the emitting area is large and the emission occurs in a broad range of directions. Synchrotrons are the brightest available sources. Soleil and SLS facilities can provide a brightness of 10^{19} and ESRF 10^{21} photons/s/mm²/mrad²/0.1%BW. In comparison, a laboratory tomograph like the EasyTom Nano has a brightness below 10^8 photons s^{-1} mm^{-2} $mrad^{-2}$ 0.1%BW (**Table 2**).

The increase of required photons with decreasing pixel size is derived from the law **[30]**:

$$\Phi \propto \frac{SNR^2}{\Delta x^4.\Delta\mu^2} \text{ (ph s}^{-1}\text{)} \quad (2)$$

where *SNR* is the signal-to-noise ratio, Δx is the voxel size and $\Delta\mu$ *is the* mean variance of absorption coefficient of the constitutive elements of the analysed object. The relation implies that compromises should be done in terms of image quality or contrast ($\Delta\mu$) in order to decrease the voxel size (Δx) and thus to increase the resolution. In fact, at a given flux and also brightness, the image quality and image contrast is restricted by the chosen voxel size. The ten times higher flux used on the Tomcat beamline (SLS

facility) allowed the voxel size to be decreased from 0.65 μm reachable on the Psiché beamline to 0.16 μm without altering the image quality. The very important brightness of the ESRF allowed reaching higher resolution of 50 nm.

Additionally, for low attenuating materials such as carbon and silicon, phase retrieval can be mandatory in order to enhance the contrast between these materials. The quality of the phase difference influences the phase retrieval process and depends mostly on the spatial coherence of the X-ray source and its monochromaticity. The more coherent and the more monochromatic the source, the better the quality of the phase retrieval. As a first approximation of the phase contrast mode, it is possible to use a Paganin-based algorithm **[31]** in order to reconstruct the first derivative of the phase and add some information about the interfaces in the bulk material on the image, while a higher brightness is required in order to perform a more complex phase retrieval calculation (second derivative of the phase), and then reconstruct a pure phase image in the Fresnel diffraction mode, like present at the ESRF end station ID16B **[32]**.

Synchrotron XRCT acquisitions were performed as follows:

(i) For acquisitions performed on electrode #2 at the Soleil beamline Psiché, 1500 projections were acquired over 180°, with a 45 ms exposure time each, and 21 reference and dark were taken regularly along the scan. The total acquisition time was around 1 minute per scan. The image reconstruction was done on site using the PyHST2 implementation of the Paganin phase retrieval calculation (delta/beta ~25) **[31]** resulting in 3D tomographic volumes of 943 × 943 × 208 μm^3 (after reframing) with an isotropic voxel size of 0.65 μm reconstructed in 32 bit floating-point from 2D projections **[33]**.

(ii) For acquisitions performed on electrode #3 at the SLS beamline Tomcat, 1001 2D projections were acquired over 180° with 700 ms of exposure time, and 21

and 11 reference and dark were taken regularly during the scan. The total acquisition time was 17 minutes per scan. Image reconstruction was achieved on site using optimized software based on Fourier methods and an ImageJ plug-in user interface and Paganin phase retrieval calculation **[34]** (delta/beta ~35) resulting in 3D tomographic volumes of 293 × 293 × 137 μm^3 (after reframing) with an isotropic voxel size of 0.163 µm reconstructed in a 32 bit floating-point from 2D projections **[35-36]**.

(iii) For acquisitions performed *in-situ* on electrodes #4 and *ex-situ* on electrodes #5 at the ESRF beamline ID16B **[37]** using holotomography **[32]**, phase contrast imaging was acquired for four different distances between the detector and the sample along the beam propagation way. 2003 projections, as well as 20 and 21 reference and dark images, were recorded on a PCO edge camera (2560×2160 pixels) along a 360° rotation with an exposure time of 300 ms per step. The total acquisition time was around 97 minutes per scan. 3D reconstructions were achieved in two steps: *(i)* phase retrieval calculation using an in-house developed octave script based on a Paganin-like approach using a delta/beta ~50 and *(ii)* filtered backprojection reconstruction using ESRF software PyHST2 **[34]**. Final volumes of 128×128×108 μm^3 (after reforming) with a voxel size of 50 nm in a 32 bit floating point were obtained.

In all cases, image analyses were performed using the ImageJ software **[38]**. Details on the procedures for the image segmentation and for their quantitative analyses (dimensional change of the electrode, volume fraction, size distribution and intra-connectivity of the segmented phases, crack growth) are presented elsewhere (see supporting information in ref. **[39]**).

3. Results and discussion

3.1. Impact of the X-ray source on the identifiable components in the electrode.

Fig. 2a-d compares lateral XRCT images acquired at different length scales with different X-ray sources on the Si-based electrodes at the pristine state. On lab tomography image obtained on electrode #1 with a voxel size of 0.8 µm and a field of view of 1358 × 1358 µm^2 (× 200 µm in thickness, not shown here) (**Fig. 2a**), Si-rich areas can be clearly identified, as the brighter regions in the electrode. The gas filled porosity is detectable as well, corresponding to the darkest regions. Some carbon fibers of the C paper substrate are slightly visible between the Si-rich regions, but have the same grey value as the rest of the electrode composed of electrolyte and Si-free solid material (*i.e.* CMC binder and carbon conductive additive).

More details can be observed in **Fig. 2b** using a more coherent and brighter source available at the synchrotron Soleil with a slightly lower voxel size of 0.65 µm and a field of view of 943 × 943 µm^2 (× 208 µm in thickness), giving access to a large overview of the composite electrode structure. The largest Si particles are now visible. Nonetheless, it is important to notice that the Si particles in electrode #2 (**Fig. 2b)** are larger with a median diameter of 2.4 µm three times higher than in electrode #1 (**Fig. 2a)**. The fibers of the C paper are visible and overall, the electrolyte phase can be now clearly differentiated from the solid phase.

With a lower voxel size of 0.16 µm reached with the Tomcat beam line at SLS on electrode #3 (**Fig. 2c**), a three times reduced field of view of 293 × 293 µm^2 (× 137 µm in thickness) is observable. This limited field of view does not allow covering the global electrode structure but it includes all of its interesting features, *i.e.* Si-rich areas, carbon fibers, pores filled with electrolyte and pores filled with gas, which can be clearly identified. The higher resolution and close-up view of the electrode allows a more precise segmentation between the electrode porosity, either filled with electrolyte

or gas, and the solid material. However, the CMC binder and carbon black additive are still not discernible and single Si particles cannot be precisely segmented.

At the highest resolution reachable at the ESRF on beam line ID16B on electrode #5 (**Fig. 2d**), a really good close up view can be obtained on the carbon fibers and Si particles with a voxel size of 0.05 µm and a field of view of 128 × 128 μm^2 (× 108 µm in thickness). This reveals here key information about the electrode structure at the submicrometric scale and especially about the morphology of the Si particles and of the porous network. Graphene nanoplatelets (GnP) used as conductive additive are also discernible.

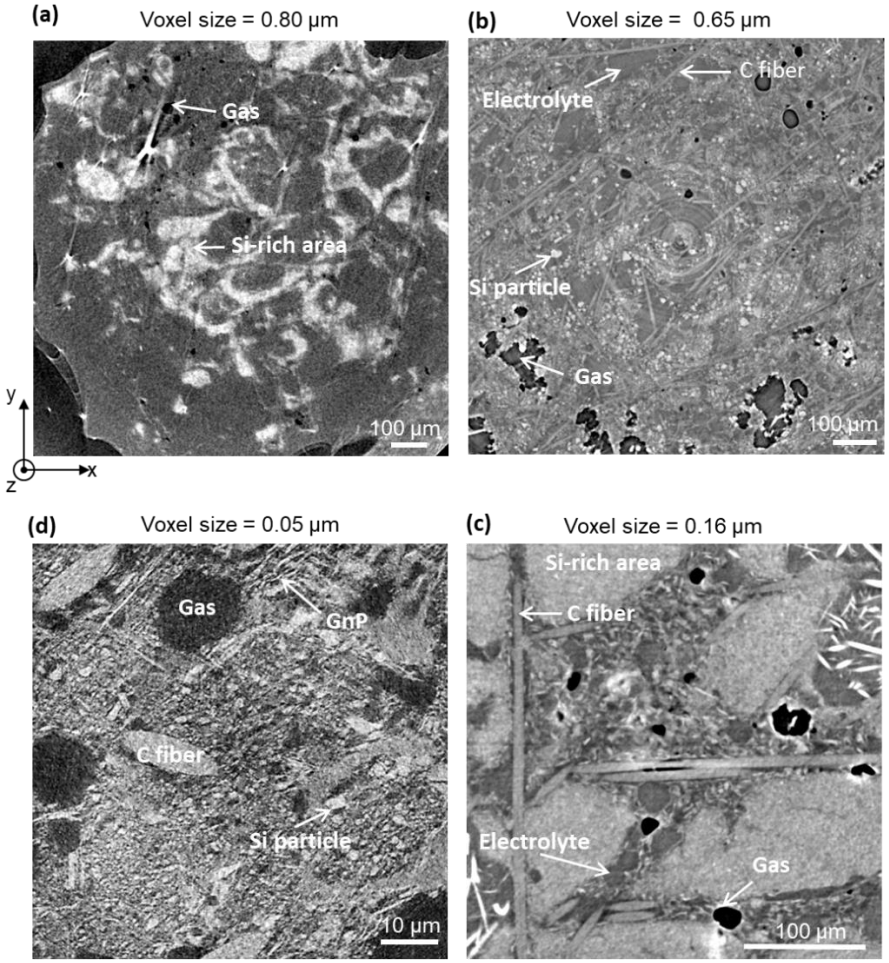

***Figure 2**. Lateral XRCT images of pristine Si-based electrodes at different scales and resolution obtained with a laboratory X-ray source on electrode* #1 *(a) and with synchrotron X-ray sources at Soleil beamline Psiché on electrode* #2 *(b), SLS beamline Tomcat on electrode* #3 *(c) and ESRF beamline ID16B on electrode* #5 *(d). The composition of the electrodes and the main features of the X-ray sources are indicated in Table 1 and 2, respectively.*

3.2. Impact of the X-ray source on the image quality (SNR and CNR).

Image quality of the 3D reconstructed renderings is evaluated thanks to the determination of the signal-to-noise ratio (SNR) and the contrast-to-noise ratio (CNR). The higher the SNR and CNR, the better the reconstructed images. The SNR can be estimated in a reconstructed image as the ratio of the mean grey level value of the voxels of interest to the standard deviation of the grey level value of the voxels in the background:

$$SNR \cong \frac{mean(voxelsofinterest)}{\sigma_{dev}(voxelsofbackground)} \quad (3)$$

The CNR is the difference of the mean grey level value of the voxels of interest and the background voxels over the standard deviation of the grey level value of the voxel of interests, as described by the equation:

$$CNR \cong \frac{mean(voxelsofinterest) - mean(voxelofbackground)}{\sigma_{dev}(voxelsofinterest)} \quad (4)$$

Fig. 3 compares lateral images of Si-electrodes for an equivalent domain size of 90 × 90 µm² obtained with the different X-ray sources. To each image corresponds a graph that represents the normalized grey value along the red dotted line on the image. SNR and CNR are calculated for each sample following equation (3) and (4) respectively. SNR is higher for the synchrotron images compared to laboratory images (SNR ~20 *vs.* ~10 respectively). This difference is due to the higher flux, coherence and monochromaticity of the synchrotron sources (**Table 2**). In fact, monochromaticity ($\Delta E/E$) is improved by a factor of ten and more using a synchrotron source and the flux can be 10^4 to 10^6 times higher. By comparing **Fig. 3a** and **3b**, having approximately the same voxel size, but SNR very different (more than a factor of two), we can conclude that twice the information from the signal is recovered for synchrotron imaging compared to laboratory measurements. Surprisingly, by comparing **Fig. 3b** and **3c,** the

SNR are almost equivalent with Soleil and SLS facilities despite a ten times higher flux at SLS (~10^{14} for SLS compared to ~10^{13} for Soleil). A CNR increase is however noticeable thanks to a lower energy (20 keV for SLS compared to 25 keV for Soleil) which increases contrast between low attenuating materials. Obviously, best resolution is obtained with the smallest voxel size obtained at the ESRF synchrotron (**Fig. 3d**) even if the SNR of this image is slightly inferior compared to those obtained for other synchrotron sources; the higher CNR insures satisfying image reliability and higher distinction between low attenuating elements.

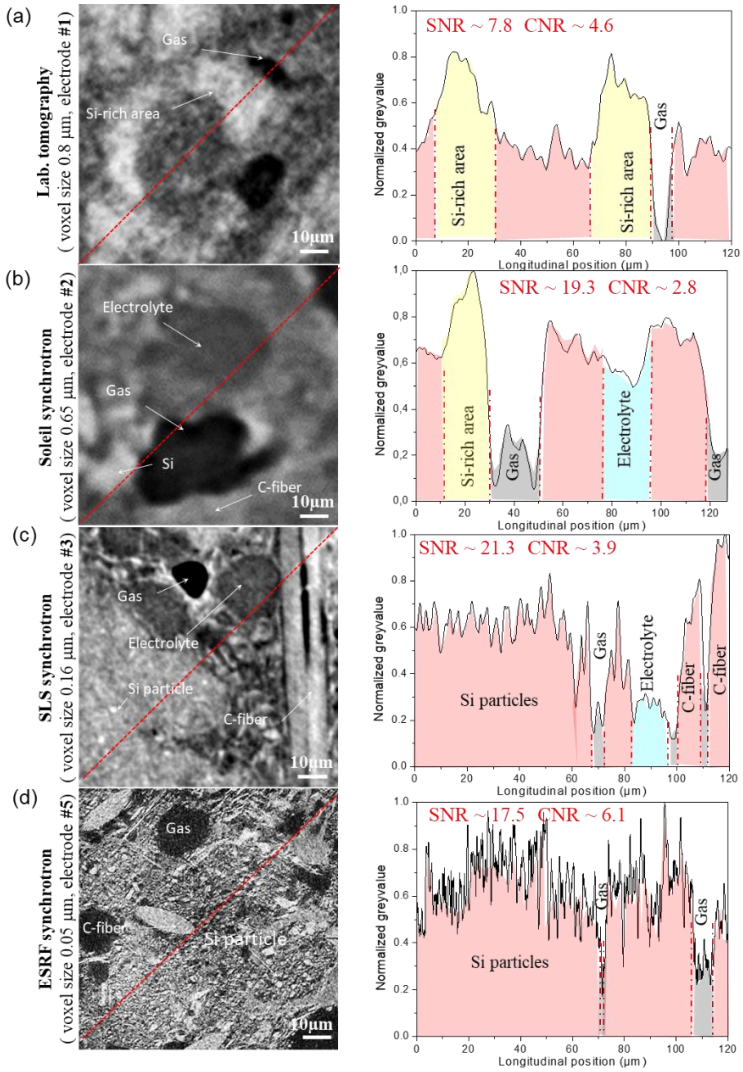

Figure 3. *Lateral images of Si-electrodes for an equivalent domain size of 90 × 90 µm² obtained with the different X-ray sources. To each image corresponds a graph (on right) that represents the normalized grey value along the red dotted line on the XRCT image.*

3.3. Representativeness of the imaged volume

The apparent heterogeneity of the present composite electrodes questions the representativeness of the morphological parameters measured from the reconstructed volume. To quantify the minimum volume required to be representative of the whole electrode volume, the mean volume fraction of pores (*i.e.* electrode porosity) and its dispersion are measured in sub-domains of different sizes of $a \times a \times 110$ µm^3 included in the total imaged volume of 943 × 943 × 208 µm^3 of the pristine electrode #2 (Soleil synchrotron with a voxel size of 0.65 µm). **Fig. 4a** presents the results with a ranging from 65 to 943 µm. 95% of the measured values are in the interval $[\overline{m} - 2\sigma; \overline{m} + 2\sigma]$ (error bar in red) and 65% are in the interval $[\overline{m} - \sigma; \overline{m} + \sigma]$ (error bar in blue) where $\overline{m}$ is the mean value and σ its standard deviation. The exact value $\overline{m^\circ}$ (46% here) is assumed to be the one measured for the whole reconstructed volume of 943 × 943 × 110 µm^3. The coloured areas in **Fig. 4a** correspond to the tolerance error interval from the exact value $\overline{m^\circ}$, *i.e.* $\left[\overline{m^\circ} - x; \overline{m^\circ} + x\right]$, with x = 5% (in grey), 10% (in red) and 15% (in green). It appears that the measured mean value $\overline{m}$ varies with the domain size but stays equal to the exact $\overline{m^\circ}$ value at ±5%. However, the lower the domain size, the larger the mean value oscillations, and the more important the measured dispersion. As seen in **Fig. 4b**, a similar tendency is observed by considering a higher spatial resolution with pristine electrode #3 (SLS synchrotron with a voxel size of 0.16 µm) and a lower whole reconstructed volume of 293 ×293 × 90 µm^3. This suggests that the voxel size has no major impact on the determined value for the minimum representative volume. The criteria that we suggest to choose for representativeness is that the average value measured should be in the ±5% interval and 95% of the measured values should equal to the exact $\overline{m^\circ}$ value at ±15%. Following these criteria the parameters estimated from

a sub-domain randomly selected in the volume should be representative of the total electrode volume. From **Fig. 4a-b**, the minimum lateral domain size found is ~200 × 200 µm^2 over the all thickness of the electrode. Smaller reconstructed volumes are likely to be non-representative and in this latter case, several measurements must be repeated and their average could be representative of the studied electrode.

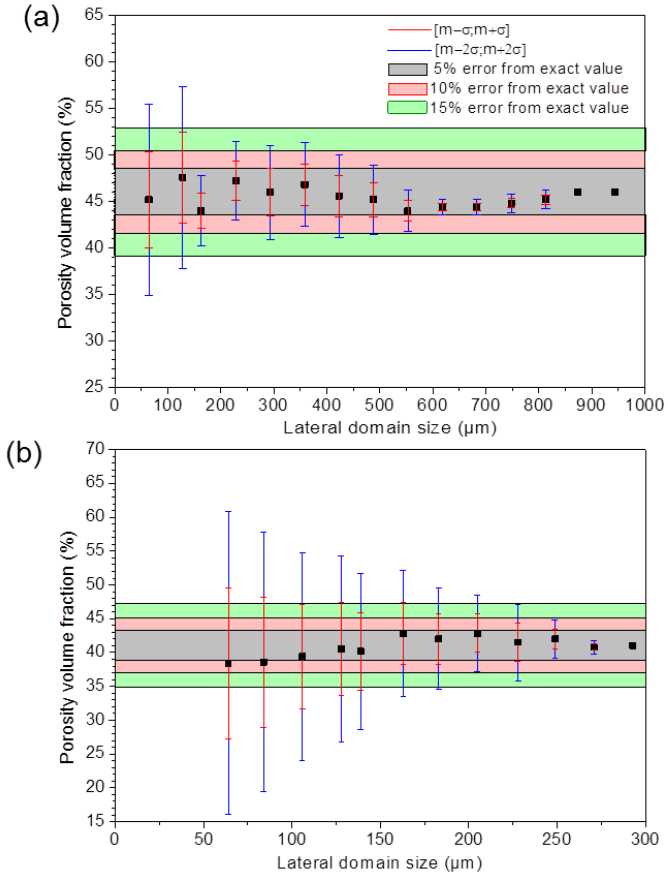

Figure 4*. Evolution of the mean volume fraction of pores and its dispersion as a function of the lateral length of the analyzed volume for the pristine electrode #2 (Soleil synchrotron, voxel size of 0.65 µm) (a) and pristine electrode #3 (SLS synchrotron, voxel size of 0.16 µm) (b).*

3.4. Expansion/contraction of the electrode

Fig. 5a shows the relative variation of the electrode thickness measured during the 1st cycle by laboratory XRCT on electrode #1 (black curve) and by synchrotron (SLS) XRCT on electrode #3 (blue curve). The electrode thickness change was determined from the displacement of the separator/electrode interface clearly

discernible on the transversal XRCT images (see below). The 1st discharge (charge) capacities of the electrodes #1 and #3 were respectively 3470 (1430) and 2884 (1968) mAh per g of silicon, corresponding to an initial coulombic efficiency (ICE) of 41 and 68%. Typical transversal *(x,z)* and lateral *(x,y)* XRCT images recorded at different steps of the 1st cycle are shown in **Fig. 5b** (electrode #1) and **Fig. 5c** (electrode #3). On the transversal images, the interface between the separator and the electrode is highlighted by a red dot line.

As shown in **Fig. 5a**, the electrode thickness variation with cycling is similar for both electrodes, which increases (decreases) almost linearly upon discharge (charge). The maximal thickness expansion observed at the end of the discharge is around 60%. An irreversible thickness increase of about 20% is measured at the end of the charge, which is indicative of irreversible modification of the electrode microstructure. The fact that the electrode thickness variations are comparable for both electrodes, despite different reconstructed volumes (~0.368 mm^3 for electrode #1 and ~0.012 mm^3 for electrode #3), tends to confirm the representativeness and homogeneity of these morphological variations. Nevertheless, the larger error bars measured for the electrode #1 traduce the fact that the resolution has an important impact on the accuracy of the measurements. For comparison, our recent *in-situ* synchrotron XRCT analyses performed with a similar electrode composition, but using a conventional Cu foil substrate, have shown a maximal thickness expansion of 72% and an irreversible thickness expansion of 25% for a 1st discharge (charge) capacity of 7.2 (4.0) mAh cm^{-2} of electrode **[39],** which are about 1.5 times higher than the present areal surface capacities. This suggests that the porous C paper substrate does not give significant improved properties to the electrode for buffering the volume expansion of the lithiated Si particles.

As XRCT is a 3D characterization method, it also offers the possibility to measure the dimensional change of the electrode along the lateral *x* and *y* axes from the displacement of reference points taken inside the electrode volume at different *z* values. Nevertheless, the error bars in the dimensional change measurements (see supplementary **Fig. S3**) indicate that the laboratory XRCT images do not allow reliable quantitative analysis of the lateral shifts compared to synchrotron sources, which are more coherent and brighter thus leading to a more accurate resolution of the different electrode features. As shown in **Fig. S3**, the dimensional change of the Si-based electrode is much lower along the lateral *x* and *y* axes (maximum of ~10-20% at the end of the discharge) than along the transversal *z* axe (maximum of ~60% at the end of the discharge). It can be explained by the fixed lateral dimensions of the electrochemical cell restricting the in-plane displacement of the electrode, whereas its out-of-plane expansion is much easier due to the softness of the separator. The in-plane fibers of the carbon paper may also constraint the lateral expansion of the electrode.

In the first stage of lithiation, the formation of gas can be detected by laboratory and synchrotron XRCT, as evidenced by the low absorbing zones pointed out by the yellow arrows in **Fig. 5b-c** at a depth-of-discharge (DOD) of 5%. Moreover, the high strains endured by the electrode contraction during delithiation lead to its cracking. Nevertheless, no crack is visible on the electrode #1 imaged by laboratory XRCT with a voxel size of 0.8 μm. By reaching a better spatial and contrast resolution thanks to synchrotron (SLS) XRCT with a voxel size of 0.16 μm (electrode #3), it is possible to discretize clearly the macro-cracks formed in the bulk of the electrode as shown in **Fig. 5c** at a state-of-charge (SOC) of 100%. These cracks are filled with electrolyte or gas. More detailed analyses on gas release and electrode cracking are presented below.

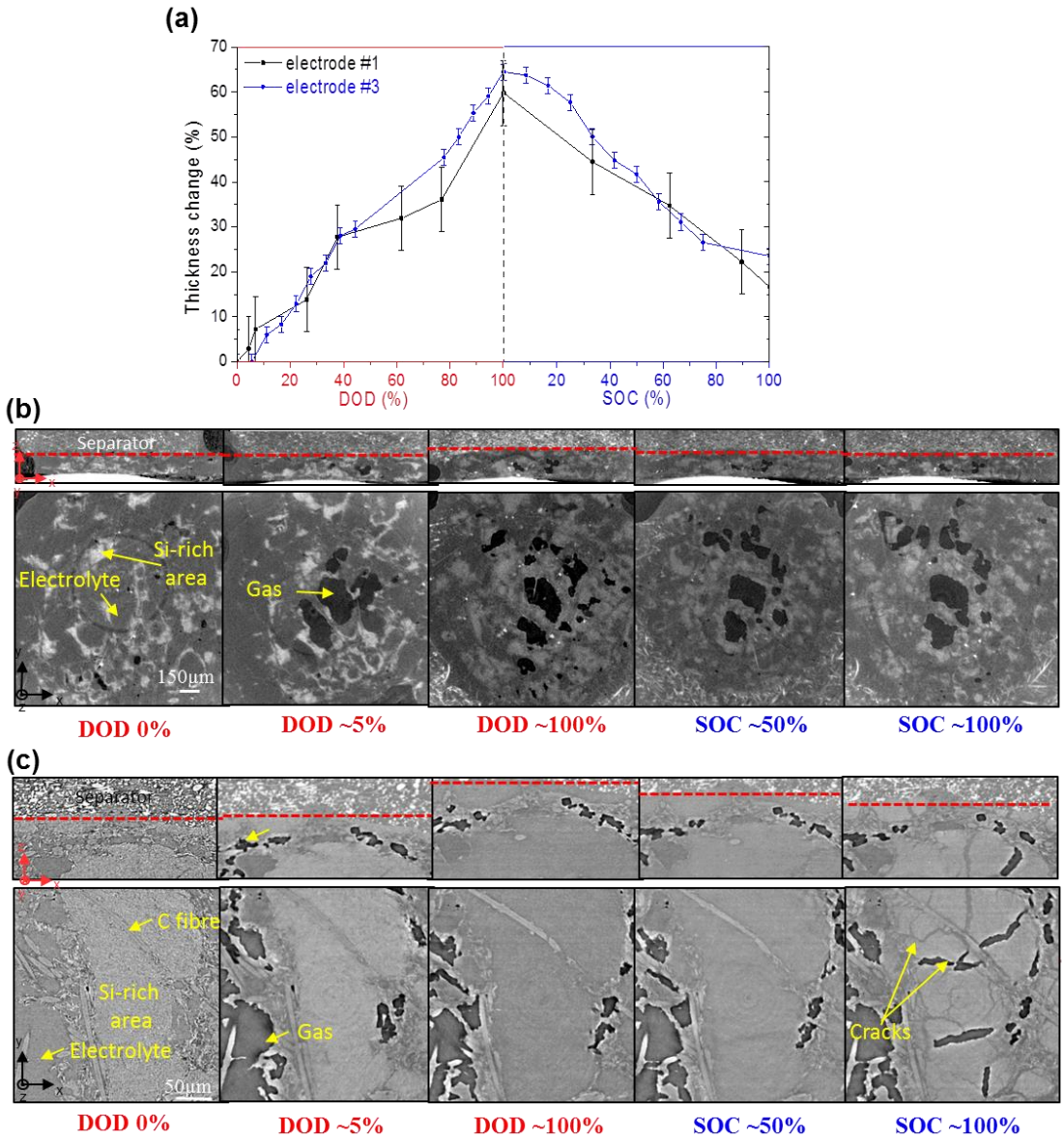

Figure 5. *Relative variation of the electrode thickness measured during the 1st cycle by laboratory XRCT on electrode #1 (black curve) and by synchrotron (SLS) XRCT on electrode #3 (blue curve) (a). Transversal (x,z) and lateral (x,y) XRCT images for different steps of the 1st cycle on electrode #1 (b) and on electrode #3 (c). The red dashed line on the transversal (x,z) images sets the electrode/separator interface.*

3.5 Impact of the FEC electrolyte additive on gas release and related SEI formation

As previously shown in **Fig. 5b-c**, some electrolyte-filled pores become much less absorbing for the X-ray beam during the initial stage of the discharge (5% DOD). We believe this is the result of gas release (*e.g.*, H_2, C_2H_4, CO_2) originating from the electrolyte decomposition during the initial SEI formation **[40]**. It is actually reasonable

to assume that the capacity recovered during this period (~200 mAh g^{-1} Si) is mostly related to the SEI formation as the electrode potential (1-0.2V) is higher than the expected Si lithiation potential and no significant electrode thickness expansion is observed during this period (**Fig. 5a** and **S3**). The formation of gas channels was also highlighted from *in-situ* synchrotron XRCT on a Si-based electrode by Sun et al. **[23]**.

It is known that the presence of FEC additive in the electrolyte has a positive impact on the SEI formation and cycle life of Si-based electrodes **[41-44]**. It appears thus relevant to perform comparative *in-situ* XRCT analyses on Si-based electrodes cycled in presence or not of FEC electrolyte additive. In this context, **Fig. 6a** compares the evolution of the volume of formed gas during the 1st discharge in the electrode #3 cycled in LP30 (black curve) and in the electrode #2 cycled in LP30 + 10%^{wt} FEC (red curve). As complementarily data, **Fig. 6b** presents the corresponding electrolyte volume variation in µL per cm^3 of electrode. The difference in the spatial resolution of the electrodes #2 and #3 (respectively 0.65 and 0.16 µm) questions nonetheless the reliability of this comparative quantitative analysis. However, this spatial resolution gap does not affect the image segmentation procedure as it depends mostly on the phase contrast resolution, which is very similar for both synchrotron X-ray sources. Additionally, the analysed volume of 0.185 mm^3 for electrode #2 and 0.012 mm^3 for electrode #3 can be considered as representative of their whole volume for both electrodes on the basis of **Fig. 4**.

As seen in **Fig. 6a**, gas formation related to the SEI formation during the initial discharge step (5% DOD) results in a rapid increase in the volume of gas-filled pores to ~140 µL cm^{-3} of electrode with the LP30 electrolyte compared to ~20 µL cm^{-3} of electrode in LP30+FEC. This in accordance with the study of Petibon et al. indicating that FEC reduction does not lead to the generation of gaseous products and prevents the

formation of methane, ethane and ethylene gas associated with the initial reduction of EC **[44]**. This is correlated to the lower electrolyte consumption highlighted by the electrolyte volume drop observed at 5% of DOD, which is 10 times lower in presence of FEC, *i.e.* 21 µL cm^{-3} *versus* 210 µL cm^{-3} in the FEC-free LP30 electrolyte (**Fig. 6b**). Subsequently, because of the electrode expansion, the gas is likely to move more freely in the electrode, which can explain the decrease of the gas volume fraction in the smallest imaged volume of electrode *#2* (**Fig. 6a**). The electrode volume expansion also draws electrolyte from the separator to the electrode, which is estimated at about 80±10 µL cm^{-3} for both electrodes (**Fig. 6b)** for a pristine electrode porosity of ~45% and a maximal thickness expansion of ~60% in both cases. Thus, one can estimate the excess of electrolyte required for accommodating both of these effects (*i.e.* SEI formation and electrode swelling) at about 280 µL cm^{-3} for the electrode #3 cycled in LP30 and 110 µL cm^{-3} for the electrode #2 cycled in LP30 + FEC. When cycled in the FEC-free electrolyte, the major part (75%) of this electrolyte volume excess is resulting from the electrolyte consumption due to the SEI formation.

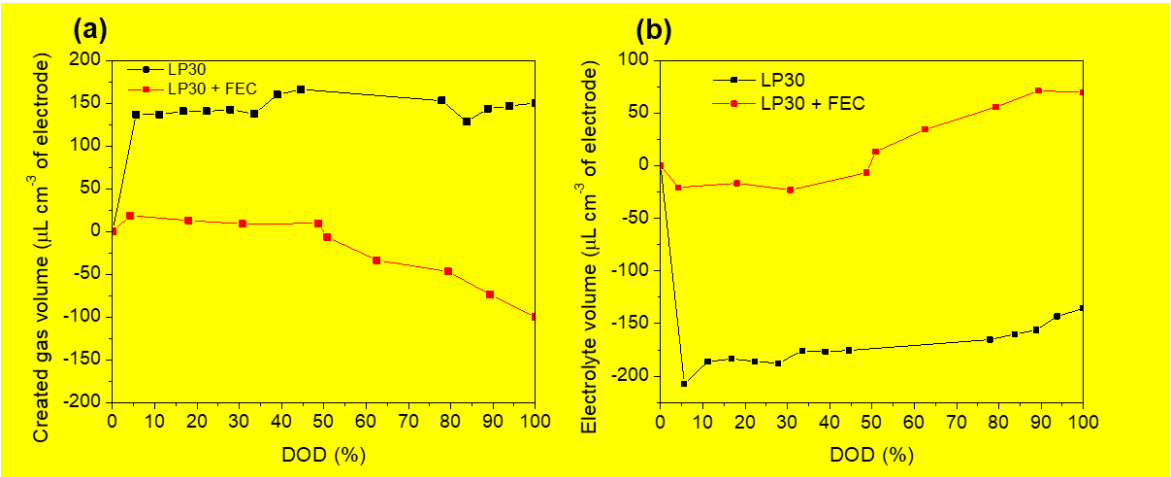

Figure 6. *Evolution during the 1st discharge of the gas volume change (a) and electrolyte volume change (b) in electrode #3 cycled in LP30 (black curves) and in electrode #2 cycled in LP30 + 10%wt FEC (red curves).*

In order to study in more detail the impact of the FEC additive on the initial SEI layer formation on the Si particles, *in-situ* synchrotron (ESRF) nano-tomography has been performed on two similar Si-based electrodes (labeled #4 in **Table 1**), one in LP30 electrolyte and the other one in LP30+ 10%^{wt} FEC, using the capillary electrochemical cell presented in **Fig. 1b**. These two electrodes were imaged at their initial state and after reaching a discharge capacity of ~250 mAh g^{-1} of Si for a total reconstructed volume of 128×128×108 μm^3 with a voxel size of 50 nm. As previously discussed, such an electrode discharge capacity extracted at a potential higher than 0.2 V vs Li/Li^+ is assumed to mainly originate from the SEI formation. Their respective dQ/dV curves recorded during the nano-XRCT experiments are shown in supplemental **Fig. S4**, highlighting the lower intensity of the EC reduction peaks in presence of FEC. Four Si particles have been selected in each electrode and their morphological evolution from 0 to 250 mAh g^{-1} of Si has been analysed as described below.

Fig. 7a-b shows the 3D rendering for one Si particle in each electrode at the pristine state and at 250 mAh g^{-1} of Si. The other analysed particles for in LP30 electrolyte and in LP30+FEC electrolyte are respectively presented in supplementary **Fig. S5-S6**. At the pristine state, the Si particles present a roughness and irregular shape with a mean diameter of a few μm, in accordance with the fact that their synthesis by high-energy ball milling results in the formation of micrometric agglomerates made of cold-welded submicrometric particles, which are partially deagglomerated during the subsequent ink mixing by magnetic stirring as previously discussed in the Experimental section. At 250 mAh g^{-1}, a slight increase (typically around 10%) of the Si particle volume is observed, whereas no particle cracking is detected. The darker regions in the grey-level 3D images correspond to the morphological difference between 0 and 250 mAh g^{-1}. For more clarity, the local thickness distribution of this expanded area is

displayed in 3D color scale images. A 2D cross-section located at the middle of the Si particle is also added. First it appears that the layer growth on the Si particle cycled in LP30 (**Fig. 7a**) is more heterogeneous in thickness than in LP30+FEC (**Fig. 7b**). This lower SEI layer uniformity in LP30 seems to be rather reproducible among the different Si particles analysed (see **Fig. S5** *vs.* **S6)**. It is also confirmed by the non-spherical ratio of the mean particle volume expansion over the mean thickness growth of the different XRCT analyzed Si particles, which is close to 4π only for the LP30+FEC formulation. In addition, the SEI layer formed on the Si particles is two times thicker in LP30 than in LP30+FEC (mean thickness of 1.4±0.4 μm and 0.65±0.3 μm, respectively). The formation of a thinner and more uniform SEI layer in the presence of FEC electrolyte additive was also observed by Etacheri et al. from *ex-situ* SEM analysis of Si nanowire electrodes and was attributed to the formation of a flexible surface film due to the presence of polycarbonates in the film resulting from the FEC decomposition **[41]**. However, in this latter case, the SEI layer was thinner (<0.2 μm) than observed here, which can be partially explained by the low surface roughness and nanowire morphology of their Si material likely to be favorable to the formation of a more compact surface film than on the present irregularly shaped and rough Si particles.

The formation of a gas bubble was also formed on top of the electrodes #4 (not shown). The size of this gas bubble was significantly smaller in presence of FEC additive, but this difference can only be qualitatively appreciated. This observation however agrees with the previous XRCT analyses performed at lower resolution and indicating a lower formation of gas in presence of FEC (**Fig. 6a**). Note that the formation of a gas bubble at the surface of the electrode in the present capillary cell results in the undesired interruption of the cycling, preventing XRCT analyses for prolonged cycling. Consequently, it was not possible to study the morphological

evolution of the Si particles (*e.g.* their cracking) associated with their lithiation from our *in-situ* synchrotron (ESRF) nano-tomography experiments.

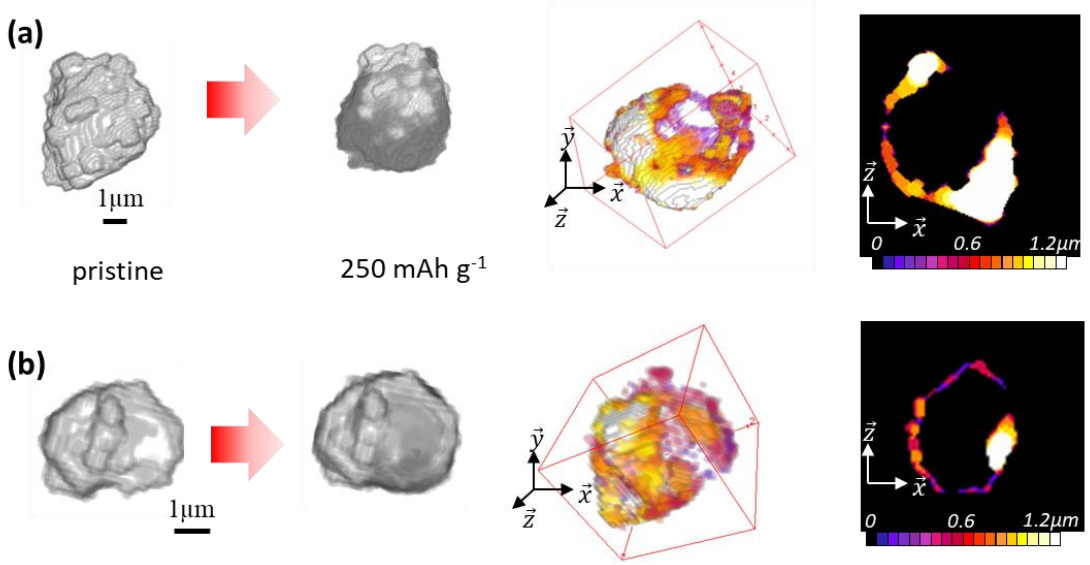

Figure 7*. 3D XRCT views of a Si particle at the pristine state and at discharge capacity of 250 mAh g^{-1} in LP30 (a) and LP30 + 10%wt FEC (b) electrolyte. The darker regions in the grey-level 3D images correspond to the morphological difference between the 0 and 250 mAh g^{-1} discharge states. The local thickness distribution of the expanded area is displayed in the 3D color-scale images and 2D color-scale images located at the middle of the Si particle.*

3.6. Electrode macro-cracking

As previously shown in **Fig. 5c**, the macro-cracks formed during the deflation (delithiation) of the Si-based electrode can be clearly identified with a coherent and bright X-ray source, and a voxel size of 0.16 µm as performed at the Tomcat beamline of SLS facility. Such a spatial resolution is however insufficient to observe the micro-cracks likely to occur within the Si particles.

The formation of macro-cracks during the 1st charge (delithiation) and their closing during the subsequent 2nd discharge (lithiation) of the electrode #3 are described in **Fig. 8a-c**. This is completed by XRCT movies, highlighting the dynamics of the electrode cracking process (see **Video 1** and **2**, Supporting Information). The crack formation at different steps of the 1st delithiation, labelled 1 to 6 on the potential curve,

and their closing at different steps of the 2nd lithiation, labelled 7 to 9 on the potential curve, are expressed in volume fractions in **Fig. 8a**. The red scale bar corresponds to gas-filled cracks and the blue ones to electrolyte-filled cracks. **Fig. 8c** presents the 3D renderings of cracks observed at each step (gas-filled in red and electrolyte-filled in blue). In order to appreciate more clearly the preferential direction of the cracks, **Fig. 8b** presents the maximum length of the largest intra-connected crack volume projected along the three Cartesian directions.

The first initiated crack, accounting for ~0.6%^{v}, is formed after reaching 40% SOC and a potential of 350 mV *vs* Li^+/Li. This crack initiation may correspond to the breaking point of the CMC binder network, associated with a contraction of the electrode thickness of about 20% (equivalent to ~30 μm) as seen in **Fig. 5a**. This crack is entirely gas filled and is mainly oriented toward the lateral *y* direction with a 145 μm maximum length. For comparison, its maximum length projected along the transversal *z* direction is around ~50 μm, which is close to the maximum value of ~65 μm reached at the end of the 1st delithiation (**Fig. 8b**). At 50% SOC, this crack is enlarging and another one (filled with electrolyte) is appearing nearby in the bulk electrode (**Fig. 8c2**) for a total volume fraction of ~0.9%^{v}. These two cracks are connecting while 60% SOC is reached (**Fig. 8c3**). The total crack volume fraction is then doubled (~1.8%^{v}) and a steep increase of its *(x,y)* lateral length is observed (**Fig. 8b)**, with a maximum length of propagation path of approximately ~290 μm, whereas only ~10 μm are added along the *z* direction. It must be kept in mind that the lateral size of the imaged region (293×293 μm) does not allow the observation of cracks longer than ~290 μm in the lateral directions, meaning that the cracks may in reality be longer in these directions. The fact that the electrode cracking preferentially occurs in the lateral directions although the electrode contraction is higher along the transversal direction (**Fig. S3b**),

may be due to the higher constraint imposed by the current collector in the *x* and *y* directions as the C paper is more flexible in the *z* direction. As the delithiation keeps forward, the cracking of the electrode intensifies and new cracks are formed in the electrode bulk leading to an important crack intra-connection of 85% and a maximal crack volume fraction of 8.4%^{v} at 100% SOC (**Fig. 8c6**). At this moment, the cracks are spread along the entire electrode length with a mean crack size around ~8 μm, forming small polygonal "islands" of ~50 μm edge. These so-called "islands" of active material are still connected to each other as the intra-connectivity of the material phase remains high (99.8% *vs* 99.9% initially), sustaining the fact that the use of a 3D structuring matrix helps reducing the electrode decohesion. Moreover, the maximum volume fraction of cracks measured at the end of 1st lithiation in this case is 40% lower than obtained for a conventional electrode deposited on a Cu current collector **[39]**. However, this high intra-connectivity of the solid phase does not preclude the electronic disconnection of some Si particles due to their displacement or cracking at the submicrometric scale, which is not detectable here due to resolution limitation. It appears also that these cracks are predominantly gas filled, as their volume fraction is three times higher than the electrolyte filled cracks. The latter are moreover mostly located at the separator/electrode interface, where the electrolyte supply is sufficient to ensure the cracks filling.

During the subsequent lithiation (steps 7 to 9), the electrode expansion is resulting in crack closing, and after reaching nearly 20% of DOD the crack volume fraction is already reduced by a half. At 45% DOD, nearly 95% of the previously formed cracks have disappeared (**Fig. 8a**). Strikingly, the decrease of the crack volume fraction is initiated in the *x* and *y* directions, while nearly no change is observed along the *z* direction before reaching 35% of DOD (**Fig. 8b**). This can be explained by the

fact that previously formed cracks have allowed the electrode to expand more freely along the lateral directions compared to the 1st lithiation. Nonetheless, this cracking process appears reversible since the electrode recovers nearly the same morphology after the 1st and 2nd lithiation. Note also that the cracking mechanism discussed in detail here in the early cycling state of the electrode can be drastically limited by replacing carbon black conductive additive by graphene nano-platelets as reported in our previous work **[24,27]**. Despite this, the capacity fade observed for this formulation after prolonged cycling needs to be assessed, and is thus discussed in more details in the subsequent part.

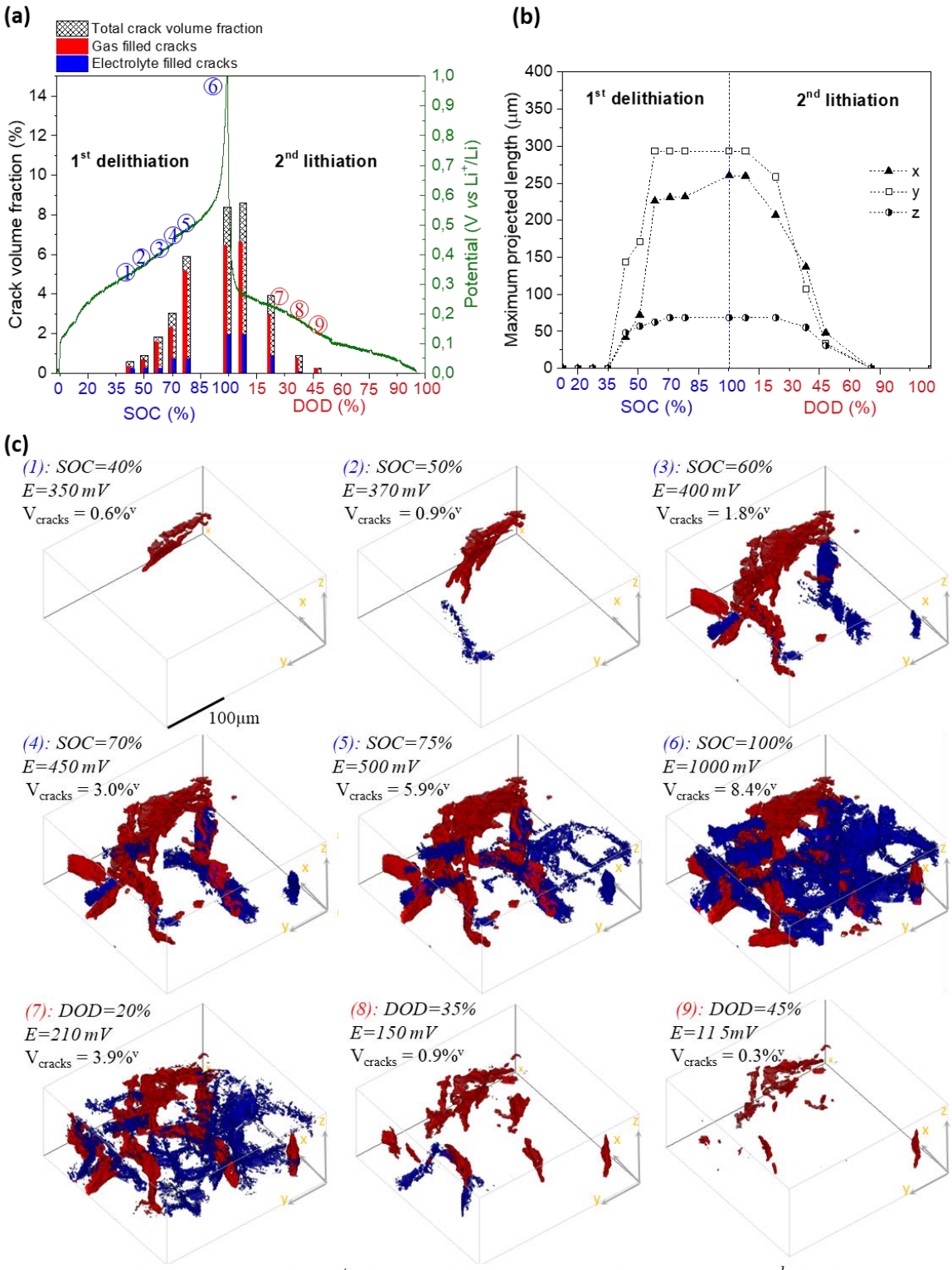

Figure 8. *Evolution during the 1st charge (delithiation) and subsequent 2nd discharge (lithiation) of the #3 electrode potential and volume fraction of macrocracks (a) and of the maximum length of the largest intra-connected crack volume projected along the x, y and z directions (b). 3D rendering of the cracks at different steps of the 1st charge and 2nd discharge (gas-filled cracks are in red and electrolyte-filled cracks in blue) (c).*

3.7. Electrode degradation after prolonged cycling

The amount of allocated synchrotron X-ray beam time (typically, a few days) is too short to perform *in-situ* XRCT experiments during prolonged cycling. Therefore, with the objective to evaluate the morphological degradation of the electrode after prolonged cycling, *ex-situ* nano-XRCT analyses were performed at ESRF (voxel size of 50 nm) on Si-based electrodes (labelled #5 in **Table 1**) at the pristine state and after 30 and 50 cycles in LP30 + 10%wt FEC using a conventional two-electrode Swagelok-type cell. Two adjacent areas were imaged for each electrode by moving the sample horizontally on the acquisition platform in order to increase the analysed volume. The total imaged volume is ~213 × 128 × 108 μm^3, which can be considered as representative of the whole electrode volume. **Fig. 9a-c** show transversal and lateral XRCT images of the electrode at the pristine state (a), after 30 cycles (b) and after 50 cycles (c). The images are here in inverted grey-scale level for more clarity, *i.e.* the more attenuating parts appears darker (*i.e.* electrode solid materials) and reciprocally the less attenuating material appears brighter (*i.e.* electrode pores). The *z* position of the lateral (*x*,*y*) image is indicated by the yellow dashed line on the transversal (*z*,*x*) image, located in the electrode bulk. For a more detailed analysis, **Fig. 10a-c** present close-up lateral images obtained from **Fig. 9a-c**. The main morphological features extracted from the quantitative analyses of the XRCT images are presented in **Table 3**.

	Pristine	30th cycle	50th cycle
Electrode thickness (μm)	~76	~96	~40-70
Electrode porosity (%)	47	28	61
Material intra-connectivity (%)	99.9	92.9	80.3
Crack volume fraction (%)	-	10	39
Crack intra-connectivity (%)	-	68.3	95.6
Median crack width (μm)	-	0.8	3.6

Table 3. *Main morphological features extracted from the ex-situ nano-XRCT analyses of the electrode #5 at the pristine state, after 30 cycles and after 50 cycles.*

At the pristine state (**Fig. 9a**), the thickness of the electrode #5 is ~76 μm and its porosity is 47%. The solid material part (*i.e.* including the Si particles, the GnP conductive additive, the CMC binder and the C fibers of the C paper) is well intra-connected (~99.9%). In the zoomed image (**Fig. 10a),** the Si particles with various shapes and sizes can be discerned in grey as well as the stringy GnP conductive additive and one C fiber of the C paper in black.

After 30 cycles, resulting in a discharge capacity decay of ~30% (see supplementary **Fig. S7**), the electrode morphology has drastically changed (**Fig. 9b**). The electrode thickness has increased to ~96 μm (+26% compared to the pristine state). Moreover, its porosity has shrunk down to 28% (-40% compared to the pristine state) in accordance with the swelling of the solid material part as noticeable on the *(x,z)* and *(x,y)* slices. This can be attributed to the accumulation of SEI products (LiF, Li_2CO_3, CH_3OLi…) in the electrode [**12,43,45**] and also to the irreversible expansion of some $SiLi_x$ particles due to their electrical disconnection. The accumulation of SEI products in the cycled electrodes is confirmed from the cross-section SEM images and corresponding EDX mapping images (Si, C, O and F elements) shown in supplemental **Fig. S8**. Additionally, the electrode appears cracked, with a crack volume fraction of ~10%^{v}. The cracking pattern is mostly constituted of elongated cracks of up to ~100 μm length with a median width of ~1 μm, separating the solid material in 25-30 μm wide "islands" with a mean thickness of ~45 μm, which is comparable to the cracked morphology observed at the end of the 1st cycle (**Fig. 8**). Despite its important volume change and cracking, the solid material in the electrode still seems to be held on together, as its intra-connectivity is still 92.9% (**Table 3**). The close-up image (**Fig. 10b)** confirms that the connection to the C paper is maintained. However, the Si particles are no longer discernible. This is attributed to the important SEI layer formed

on their surface and in the electrode micro-porosity, presumably helping thus holding on together the electrode solid materials. However, this mechanical connection does not preclude their electrical disconnection, as the SEI layer is not electrically conductive.

At the 50th cycle, the electrode discharge capacity decay reaches ~40% (see supplementary **Fig. S7**) and its morphological degradations keep intensifying **(Fig. 9c)**. The electrode decohesion is visible: an upper part of the electrode has detached from the rest during the electrode rinsing step, as indicated by the delaminated red area in **Fig. 9c**. The electrode thickness is then reduced down to ~40-70 μm and its porosity is increased up to ~61%. Moreover, the solid material areas are highly pulverized owing to the increased crack density, resulting in a decrease of the material phase intra-connectivity down to 80.3% (**Table 3**). The crack volume fraction after 50 cycles is increased up to ~39%, and their median width size is also four times larger (~3.6 μm). Besides, its intra-connectivity has increased between the 30th and the 50th cycle, from 68.3 to 95.6%, traducing the higher crack density as qualitatively observed in **Fig. 9c**. The material phase is thus segregated into smaller "islands" of 5-10 μm width and an average thickness of ~10 μm. This can be appreciated more clearly on the close-up image in **Fig. 10c**. At this step of cycling, the electrode is much more disposed to lose active material by electrode delamination as previously reported [**13**]. Nonetheless, the electrode compression by a spring in the electrochemical cell is likely to keep its mechanical integrity in some extent and allow different segregated material parts to reconnect upon cycling, as suggested by the capacity jump events observed at different periods of cycling (especially from ~25 cycles) in supplementary **Fig. S7** and also reported by Nguyen *et al.* **[46]**. Finally, the X-ray contrast appears darker after 50 cycles (**Fig. 9c**) than after 30 cycles (**Fig. 9b**), meaning that it attenuates the beam harder and

that, its constituting solid material gets presumably denser as cycling progresses. This can be explained by the fact that prolonged cycling causes the submicrometric porosity (*i.e.* interstices between the Si particles) to be filled with accumulated SEI products. This is also supported by the structural changes observed by SEM at the silicon particle level on these electrodes (see supplementary **Fig. S9**). Their morphology becomes more fractal after prolonged cycling and their SEI covering appears denser, especially after 50th cycle. This implies that the major challenge facing prolonged Si-based electrode cycling lies in minimizing the SEI growth, especially through the development of more efficient electrolyte additives than FEC.

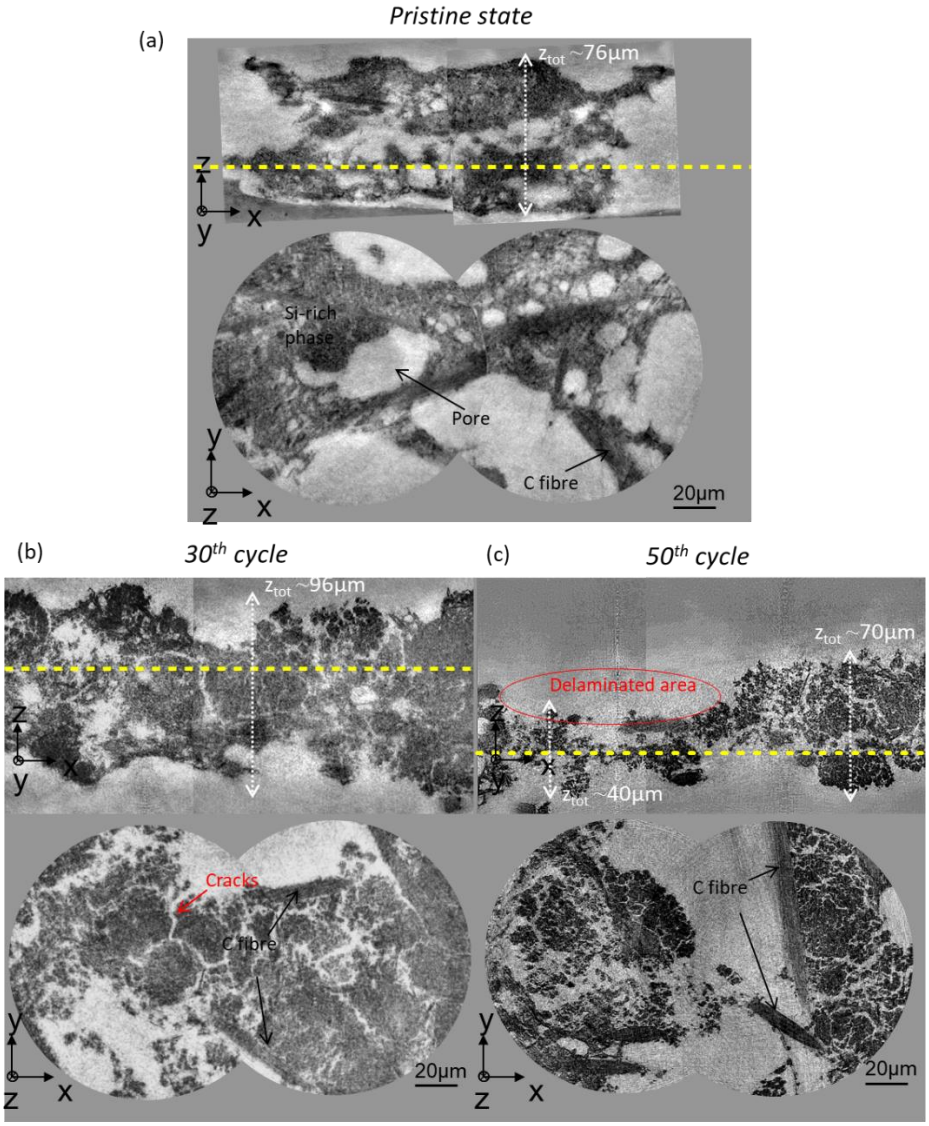

Figure 9. *Transversal and lateral ex-situ XRCT images of the electrode #5 at the pristine state (a), after 30 cycles (b) and after 50 cycles (c). Rendering are in inverted greyscale look up table*

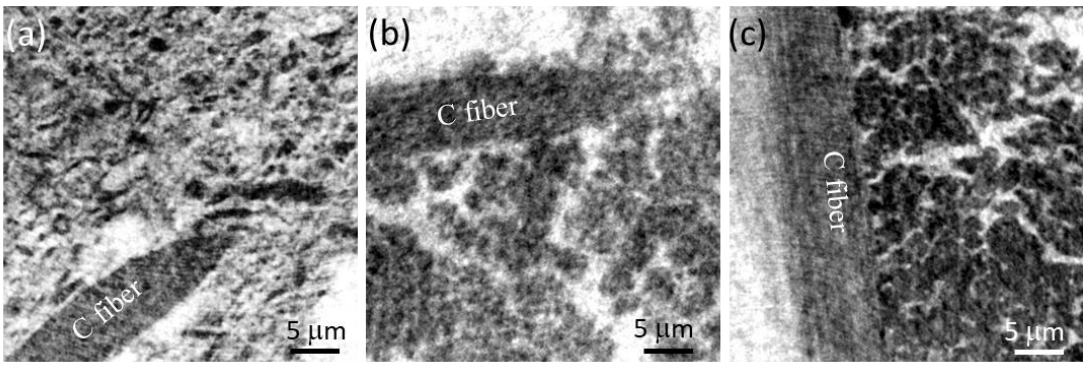

Figure 10. *Lateral close-up images (36×36 µm^2) extracted from the XRCT images of Fig. 9. at the pristine state (a), after 30 cycles (b) and after 50 cycles (c).Rendering are with inverted greyscale look up table.*

4. Conclusion

This study has shown that XRCT is a powerful *in-situ* characterization method for visualizing and quantifying the morphological degradations of Si-based electrodes from the microscale (*i.e.* at the composite electrode level) to the nanoscale (*i.e.* at the Si particle level). It was highlighted that the XRCT resolution limit strongly depends on the X-ray source and the electrochemical cell configuration. A spatial resolution as low as 50 nm can only be reached by using a very bright X-ray source such as available at the European Synchrotron Radiation Facility. It was also shown that a minimum lateral domain size of ~200 × 200 µm^2 over the all electrode thickness must be imaged to be well representative of the total electrode volume. With a synchrotron X-ray source, the porous network of the electrode (filled or free of electrolyte) can be clearly differentiated from the solid components of the electrode (Si particles, binder and conductive additive). Differentiation (segmentation) of the solid components is more challenging due to their small size and low X-ray contrast. However, micrometric Si particles are discernible. After appropriate image processing, segmentation and analysis

procedures, valuable qualitative and quantitative information on the 3D morphological evolution of the electrode can be obtained:

(i) The expansion/contraction of the electrode associated with its lithiation/delithiation mainly occurs in the transversal direction (electrode thickness) and is partially reversible. The electrode volume expansion upon discharge also draws electrolyte from the separator to the electrode.

(ii) During the initial stage of discharge, the formation of gas and the consumption of electrolyte attributed to the SEI formation can be quantified. They are both significantly decreased in presence of FEC electrolyte additive. Moreover, the initial SEI layer formed on the Si particles seems to be thinner and more uniform in the presence of FEC.

(iii) The dynamics of the formation of macro-cracks in the electrode during its charge and their closing during the subsequent discharge has been studied. It appears that the macrocracks grow preferentially in the lateral plan of the electrode and they are mainly gas-filled.

(iv) The electrode cracking and decohesion as well as the SEI thickening are exacerbated upon prolonged cycling as confirmed from *post-mortem* XRCT and SEM analyses of the Si-based electrodes after 30 and 50 cycles. This suggests that the excessive SEI growth despite the presence of FEC electrolyte additive plays a key role in the morphological degradation of the electrode.

Acknowledgments

The authors thank the Natural Sciences and Engineering Research Council (NSERC) of Canada for its financial support (Grant No. RGPIN-2016-04524). The authors also

thank M. Mokhtari at SLS, G. Meyruey and Q. Lemarie at Soleil, and S. Labouré at ESRF for their help for the XRCT measurements.

Reference

[1] B. Yang, Y.-P. He, J. Irsa, J.B. Ratchford, Y.-P Zhao, Effects of composition-dependent modulus, finite concentration and boundary constraint on Li-ion diffusion and stresses in a bilayer Cu-coated Si-nano-anode. J. Power Sources 204 (2012) 168-176.

[2] S.J. Cooper, D.S. Eastwood, J. Gelb, G. Damblanc, D.J.L. Brett, R.S. Bradley, P.J. Withers, P.D. Lee, A.J. Marquis, N.P. Brandon, P.R. Shearing, Image based modelling of microstructural heterogeneity in $LiFePO_4$ electrodes for Li-ion batteries, J. Power Sources 247 (2014) 1033-1039.

[3] C. L. Cobb & M. Blanco, Modeling mass and density distribution effects on the performance of co-extruded electrodes for high energy density lithium-ion batteries, J. Power Sources 249 (2014) 357-366.

[4] Y. K. Chen-Wiegart, R. DeMike, C. Erdonmez, K. Thornton, S.A. Barnett, J. Wang, Tortuosity characterization of 3D microstructure at nano-scale for energy storage and conversion materials, J. Power Sources 249 (2014) 349-356.

[5] M. Ebner, D. Chung, R.E. García, V. Wood, Tortuosity anisotropy in lithium-ion battery electrodes, Adv. Energy Mater. 4 (2014) 1301278.

[6] G.M. Goldin, A.M. Colclasure, A.H. Wiedemann, R.J. Keeb, Three-dimensional particle-resolved models of Li-ion batteries to assist the evaluation of empirical parameters in one-dimensional models, Electrochim. Acta 64 (2012) 118-129.

[7] J. W. Choi, D. Aurbach, Promise and reality of post-lithium-ion batteries with high energy densities, Nat. Rev. Mater. 1 (2016) 16013.

[8] M. A. Gialampouki, J. Hashemi, A. A. Peterson, The Electrochemical Mechanisms of Solid−Electrolyte Interphase Formation in Lithium-Based Batteries, J. Phys. Chem. C 123 (2019) 20084−20092.

[9] B. Horstmann, F. Single, A. Latz, Review on multi-scale models of solid-electrolyte interphase formation, Current Opinion in Electrochemistry 13 (2019) 61–69.

[10] M.T. McDowell, S.W. Lee, J.T. Harris, B.A. Korgel, C. Wang, W.D. Nix, Y. Cui, In situ TEM of two-phase lithiation of amorphous silicon nanospheres, Nano Lett. 13 (2013) 758-764.

[11] X. H. Liu, L. Zhong, S. Huang, S. X. Mao, T. Zhu, J.Y. Huang, Size-dependent fracture of silicon nanoparticles during lithiation, ACS Nano. 6 (2012) 1522-1531.

[12] A. Etiemble, A. Tranchot, T. Douillard, H. Idrissi, E. Maire, L. Roué, Evolution of the 3D microstructure of a Si-based electrode for Li-ion batteries investigated by FIB/SEM tomography, J. Electrochem. Soc. 163 (2016) A1550-A1559.

[13] C. R. Hernandez, A. Etiemble, T. Douillard, D. Mazouzi, Z. Karkar, E. Maire, D. Guyomard, B. Lestriez, L. Roué, A Facile and Very Effective Method to Enhance the Mechanical Strength and the Cyclability of Si-Based Electrodes for Li-Ion Batteries, Adv. Energy Mater. 8 (2018) 1701787.

[14] F. Tariq, V.Yufit, D.S. Eastwood, Y. Merla, M. Biton, B. Wu, Z. Chen, K. Freedman, G. Offer, E. Peled, P.D. Lee, D. Golodnitsky, N. Brandon, In-operando x-ray tomography study of lithiation induced delamination of Si based anodes for lithium-ion batteries, ECS Electrochem. Lett. 3 (2014) A76-A78.

[15] J. Gonzalez, K. Sun, M. Huang, J. Lambros, S. Dillon, I. Chasiotis, Three dimensional studies of particle failure in silicon based composite electrodes for lithium ion batteries, J. Power Sources 269 (2014) 334-343.

[16] C. Zhao, T. Wada, V. De Andrade, D. Gursoy, H. Kato, Y.K. Chen-Wiegart, Imaging of 3D Morphological Evolution of Nanoporous Silicon Anode in

Lithium Ion Battery by X-Ray Nano-Tomography, Nano Energy 52 (2018) 381-390.

[17] P. Pietsch, M. Hess, W. Ludwig, J. Eller, V. Wood, Combining operando synchrotron X-ray tomographic microscopy and scanning X-ray diffraction to study lithium ion batteries, Sci. Rep. 6 (2016) 27994.

[18] F. Sun, H. Markötter, K. Dong, I. Manke, A. Hilger, N. Kardjilov, J. Banhart, Investigation of failure mechanisms in silicon based half cells during the first cycle by micro X-ray tomography and radiography, J. Power Sources 321 (2016) 174-184.

[19] J.M. Paz-Garcia, O.O. Taiwo, E.Tudisco, D.P. Finegan, P.R. Shearing, D.J.L. Brett, S.A. Hall, 4D analysis of the microstructural evolution of Si-based electrodes during lithiation: Time-lapse X-ray imaging and digital volume correlation, J. Power Sources 320 (2016) 196-203.

[20] P. Pietsch, D. Westhoff, J. Feinauer, J. Eller, F. Marone, M. Stampanoni, V.Schmidt, V. Wood, Quantifying microstructural dynamics and electrochemical activity of graphite and silicon-graphite lithium ion battery anodes, Nat. Commun. 7 (2016) 12909.

[21] L. Zielke, F. Sun, H. Markötter, A. Hilger, R. Moroni, R. Zengerle, S Thiele, J. Banhart, I. Manke, Synchrotron X-ray tomographic study of a silicon electrode before and after discharge and the effect of cavities on particle fracturing, Chem. Electro Chem. 3 (2016) 1170-1177.

[22] V. Vanpeene, A. Etiemble, A. Bonnin, E. Maire, L. Roué, In-situ X-ray tomographic study of the morphological changes of a Si/C paper anode for Li-ion batteries, J. Power Sources 350 (2017) 18-27.

[23] F. Sun, H. Markötter, I. Manke, A. Hilger, N. Kardjilov, J. Banhart, Three-dimensional visualization of gas evolution and channel formation inside a lithium-ion battery, ACS Appl. Mater. Interfaces 8 (2016) 7156–7164.

[24] V. Vanpeene, A. King, E. Maire, L. Roué, In situ characterization of Si-based anodes by coupling synchrotron X-ray tomography and diffraction, Nano Energy 56 (2019) 799-812.

[25] P. Pietsch, V. Wood, X-Ray Tomography for Lithium Ion Battery Research: A Practical Guide, Annual Review of Materials Research 47 (2017) 451-479.

[26] M. Gauthier, D. Mazouzi, D. Reyter, B. Lestriez, P. Moreau, D. Guyomard, L. Roué, A low-cost and high performance ball-milled Si-based negative electrode for high-energy Li-ion batteries, Energy Environ. Sci. 6 (2013) 2145-2155.

[27] Z. Karkar, D. Mazouzi, C.R. Hernandez, D. Guyomard, L. Roué, B. Lestriez, Threshold-like dependence of silicon-based electrode performance on active mass loading and nature of carbon conductive additive, Electrochim. Acta 215 (2016) 276-288.

[28] D. Mazouzi, B. Lestriez, L. Roué, D. Guyomard, Silicon composite electrode with high capacity and long cycle life, Electrochem. Solid-State Lett. 12 (2009) A215-A218.

[29] A. Tranchot, H. Idrissi, P. X. Thivel, L. Roué, Impact of the slurry pH on the expansion/contraction behavior of silicon/carbon/carboxymethylcellulose electrodes for Li-ion batteries, J. Electrochem. Soc. 163 (2016) A1020-A1026.

[30] U. Bonse, F. Busch, X-ray computed microtomography using synchrotron radiation, Prog. Biophys. Molec. Bio. 65 (1996) 133-169.

[31] D.M. Paganin, Coherent X-Ray Optics, Vol. 6 of Oxford series on synchrotron radiation, Oxford University Press, Oxford, 2006.

[32] P. Cloetens, W. Ludwig, J. Baruchel, Holotomography: Quantitative phase tomography with micrometer resolution using hard synchrotron radiation X rays, Appl. Phys. Lett. 75 (1999) 2912-2914.

[33] A. Mirone, E. Brun, E. Gouillart, P. Tafforeau, J. Kieffer, The PyHST2 hybrid distributed code for high speed tomographic reconstruction with iterative reconstruction and a priori knowledge capabilities, Nucl. Instrum. Methods B 324 (2014) 41-48.

[34] C. Hintermüller, F. Marone, A. Isenegger, M. Stampanoni, Image processing pipeline for synchrotron-radiation-based tomographic microscopy, J. Synchrotron Rad. 17 (2010) 550-559.

[35] F. Marone, B. Münch, M. Stampanoni, Fast reconstruction algorithm dealing with tomography artifacts, SPIE Proc. 7804 (2010) 780410.

[36] F. Marone, M. Stampanoni, Regridding reconstruction algorithm for real time tomographic imaging, J. Synchrotron Rad. 19 (2012) 1029-1037.

[37] G. Martínez-Criado, J. Villanova, R. Tucoulou, D. Salomon, J.-P. Suuronen, S. Labouré, C. Guilloud, V. Valls, R. Barrett, E. Gagliardini, Y. Dabin, R. Baker, S. Bohic, C. Cohen and J. Morse, ID16B: a hard X-ray nanoprobe beamline at the ESRF for nano-analysis, J. Synchrotron Rad. 23 (2016) 344–352.

[38] J. Schindelin, I.Arganda-Carreras, E. Frise, V. Kaynig, M. Longair, T. Pietzsch, S. Preibisch, C. Rueden, S. Saalfeld, B. Schmid, J.-Y. Tinevez, D. J. White, V. Hartenstein, K. Eliceiri, P. Tomancak, A. Cardona, Fiji: an open-source platform for biological-image analysis, Nat. Methods 9 (2012) 676-682.

[39] V. Vanpeene, J. Villanova, A. King, B. Lestriez, E. Maire, L. Roué, Dynamics of the morphological degradation of Si-based anodes for Li-ion batteries

characterized by in-situ synchrotron X-ray tomography, Adv. Energy Mater. 9 (2019) 1803947.

[40] L.D. Ellis, J.P. Allen, L.M. Thompson, J.E. Harlow, W.J. Stone, I.G. Hill, J.R. Dahn, Quantifying, Understanding and Evaluating the Effects of Gas Consumption in Lithium-Ion Cells, J. Electrochem. Soc. 164 (2017) A3518-A3528.

[41] V. Etacheri, O. Haik, Y. Goffer, G.A. Roberts, I.C. Stefan, R. Fasching, D. Aurbach, Effect of fluoroethylene carbonate (FEC) on the performance and surface chemistry of Si-nanowire Li-ion battery anodes, Langmuir 28 (2012) 965-976.

[42] C. Xu, F. Lindgren, B. Philippe, M. Gorgoi, F. Björefors, K. Edström, T. Gustafsson, Improved performance of the silicon anode for Li-ion batteries: understanding the surface modification mechanism of fluoroethylene carbonate as an effective electrolyte additive, Chem. Mater. 27 (2015) 2591-2599.

[43] D. Mazouzi, N. Delpuech, Y. Oumellal, M. Gauthier, M. Cerbelaud, J. Gaubicher, N. Dupré, P. Moreau, D. Guyomard, L. Roué, B. Lestriez, New insights into the silicon-based electrode's irreversibility along cycle life through simple gravimetric method, J. Power Sources 220 (2012) 180-184.

[44] R. Petibon, V. L. Chevrier, C. P. Aiken, D. S. Hall,S. R. Hyatt, R. Shunmugasundaram, J. R. Dahn, Studies of the Capacity Fade Mechanisms of LiCoO2/Si-Alloy: Graphite Cells, J. Electrochem. Soc. 163 (2016) A1146-A1156.

[45] Y. Oumellal, N. Delpuech, D. Mazouzi, N. Dupré, J. Gaubicher, P. Moreau, P. Soudan, B. Lestriez, D. Guyomard, The failure mechanism of nano-sized Si-

based negative electrodes for lithium ion batteries, J. Mater. Chem. 21 (2011) 6201-6208.

[46] B.P.N. Nguyen, J. Gaubicher, B. Lestriez, Analogy between electrochemical behaviour of thick silicon granular electrodes for lithium batteries and fine soils micromechanics, Electrochim. Acta 120 (2014) 319-326.